

# Superconducting Acoustogalvanic Effect in Twisted Transition Metal Dichalcogenides

Tsugumi Matsumoto,<sup>1,\*</sup> Ryotaro Sano,<sup>1,2</sup> Youichi Yanase,<sup>1</sup> and Akito Daido<sup>1,3</sup>

<sup>1</sup>*Department of Physics, Graduate School of Science, Kyoto University, Kyoto 606-8502, Japan*

<sup>2</sup>*Institute of Solid State Physics, University of Tokyo, Kashiwa 277-8581, Japan*

<sup>3</sup>*Department of Physics, Hong Kong University of Science and Technology, Clear Water Bay, Hong Kong, China*  
(Dated: June 10, 2025)

The recently discovered twisted bilayer superconductors have suffered from a lack of reliable methods for identifying their nontrivial pairing symmetries and quantum geometry. In this study, we propose nonlinear responses driven by surface acoustic waves as a novel probe to access exotic Bogoliubov quasiparticles in such superconductors. Our approach is particularly suitable for addressing the superconducting gap structure as the gap energies in these systems typically lie within the frequency range of surface acoustic waves, and thus paves the way toward the experimental identification of exotic superconducting states especially in low- $T_c$  superconductors.

*Introduction.*— The recent discovery of twisted multilayer van der Waals (vdW) superconductors with the honeycomb structure, exemplified by magic angle twisted bilayer graphene (MATBG) [1] and twisted WSe<sub>2</sub> (tWSe<sub>2</sub>) [2, 3], has opened avenues for realizing various exotic superconducting states that have long been sought after. Particularly in tWSe<sub>2</sub>, chiral and nematic superconductivity—which spontaneously break time-reversal and rotational symmetries, respectively—are promising candidates for its observed superconducting state [4, 5]. Towards their experimental identification, it is essential to clarify the wave-function properties of Cooper pairs and Bogoliubov quasiparticles, namely their symmetry and quantum geometry. However, conventional probes such as optical responses and heat transport face a difficulty in accessing these properties due to extremely low critical temperatures as well as the two-dimensional nature. Therefore, developing novel measurement methods more suitable for atomically thin vdW superconductors is highly desired.

Nonlinear responses have recently established their profound connections to the symmetry and quantum geometry inherent in normal-state Bloch electrons [6, 7]. This concept has now been extended to superconducting states with particular emphasis on nonlinear optical responses [8–15]. By activating the hidden quantum-geometric properties of Bogoliubov quasiparticles, nonlinear responses may provide a powerful tool for studying exotic superconducting states. However, the electromagnetic fields suffer from a fundamental limitation intrinsic to superconductors: the coupling between the vector potential and momentum enters with opposite signs in the particle and hole sectors. This fact sharply contrasts with the normal-state counterpart, and thus prevents nonlinear optical responses from directly capturing the quantum geometry of Bogoliubov quasiparticles.

Surface acoustic waves (SAWs) are highly directional mechanical vibrations that propagate along the surface of elastic media. SAWs serve as a vibrational probe at the nanoscale, offering a compelling platform for simultaneously modulating materials via surfing carriers in 2D

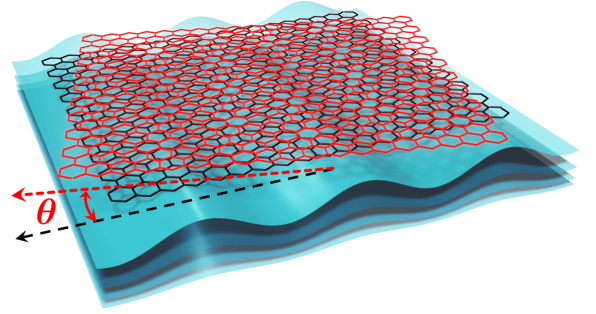


FIG. 1. Schematics of the superconducting acoustogalvanic effect in twisted vdW materials with a twist angle  $\theta$ . A spatial modulation of the hopping energies due to strain mimics the role of artificial gauge fields for Bogoliubov quasiparticles in a honeycomb lattice.

materials through piezoelectric and strain fields [16–20]. Specifically in honeycomb systems, a spatial modulation of the hopping energies due to strain mimics the role of artificial gauge fields [21–29], exerting a driving force even on charge-neutral quasiparticles [30–34]. Therefore, the strain-induced gauge fields have the potential to replace the role of electromagnetic fields and temperature gradients in the study of atomically thin vdW materials, owing to their remarkable mechanical flexibility. Furthermore, these strain gauge fields work at the two valley points in the opposite direction, thereby activating the valley degrees of freedom (DOF). This valley-contrasting nature offers a distinct advantage in overcoming the electromagnetic limitation in honeycomb superconductors, especially in systems where Cooper pairs are formed between electrons located at the opposite valley points.

In this Letter, we propose the *superconducting acoustogalvanic effect*—a nonlinear response driven by SAWs—as a novel probe of the pairing symmetry and quantum geometry of Bogoliubov quasiparticles in two-dimensional honeycomb superconductors including those formed with a twisted bilayer (Fig. 1). The unique combination of mechanical tunability and valley-contrasting

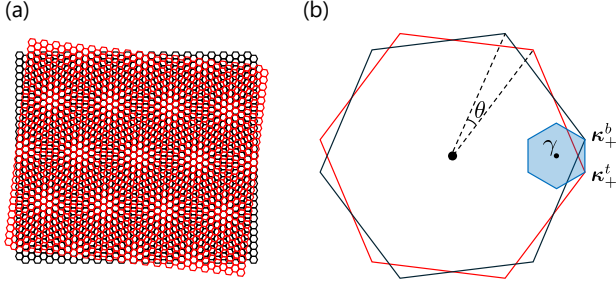


FIG. 2. Schematics of (a) the moiré superlattice and (b) the corresponding reciprocal space with a twist angle  $\theta$ . The red and black sheets represent the top and bottom layers, respectively. The blue area is the folded moiré Brillouin zone.

pseudo-gauge fields elevates SAWs as a promising tool for probing the symmetry and quantum-geometry aspects in atomically thin superconductors. In particular, we focus on inter-valley pairing in tWSe<sub>2</sub>, where the valley-contrasting nature of strain fields allows selective activation of quantum-geometric responses that are otherwise hidden in conventional electromagnetic probes. We show that SAWs can induce a pronounced nonlinear response, tightly linked to the underlying quantum geometry of the superconducting state, and further discuss its potential as a remarkable tool for investigating exotic superconducting states in vdW materials.

*Model.*— To investigate SAWs responses in honeycomb superconductors, we examine an AA-stacked bilayer WSe<sub>2</sub> with a small twist angle  $\theta$  [Fig. 2 (a)]. We begin with the standard continuum model [35] defined in the moiré Brillouin zone (MBZ) as depicted in Fig. 2 (b),

$$\hat{H}_\tau = \begin{pmatrix} H_{\tau,b}(\hat{\mathbf{k}}) + \Delta_b(\hat{\mathbf{r}}) & T_\tau(\hat{\mathbf{r}}) \\ T_\tau^\dagger(\hat{\mathbf{r}}) & H_{\tau,t}(\hat{\mathbf{k}}) + \Delta_t(\hat{\mathbf{r}}) \end{pmatrix}, \quad (1)$$

where  $\tau = \pm$  and  $l = b/t = \pm$  denote the valley and layer DOF. Owing to the spin-orbit coupling, the spin of the  $\tau = \pm$  valley is locked to  $\uparrow$  and  $\downarrow$ , respectively, and are kept implicit. Here,  $\hat{H}_{\tau,l}$  is the Hamiltonian of each monolayer, and  $\Delta_l(\hat{\mathbf{r}})$  and  $T_\tau(\hat{\mathbf{r}})$  are intralayer and interlayer potentials, respectively. These components are given by

$$H_{\tau,l}(\hat{\mathbf{k}}) = -\frac{\hbar^2}{2m^*}(\hat{\mathbf{k}} - \boldsymbol{\kappa}_{\tau,l})^2 - l\frac{V_z}{2} - \mu, \quad (2a)$$

$$\Delta_l(\hat{\mathbf{r}}) = V \sum_{j=1,2,3} e^{i(\mathbf{g}_j \cdot \hat{\mathbf{r}} + l\psi)} + \text{h.c.}, \quad (2b)$$

$$T_\tau(\hat{\mathbf{r}}) = w(1 + e^{+i\tau\mathbf{g}_2 \cdot \hat{\mathbf{r}}} + e^{-i\tau\mathbf{g}_3 \cdot \hat{\mathbf{r}}}), \quad (2c)$$

where  $m^* = 0.43m_e$  is the effective mass,  $\mu$  is the chemical potential, and  $\boldsymbol{\kappa}_{\tau,l} = [4\pi\tau/3L_M](\sqrt{3}/2, l/2)$  are the momentum shifts. Here, the moiré lattice constant and the reciprocal lattice vectors in the MBZ are given by,  $L_M = a_0/[2\sin(\theta/2)]$  and  $\mathbf{g}_j =$

$\frac{4\pi}{\sqrt{3}L_M} \left( \cos \frac{2(j-1)\pi}{3}, \sin \frac{2(j-1)\pi}{3} \right)$ . Throughout this Letter, we set the parameters:  $(\theta, V, \psi, w, V_z, \mu) = (5^\circ, 9 \text{ meV}, 128^\circ, 18 \text{ meV}, 43.75 \text{ meV}, -13 \text{ meV})$  [3, 36, 37] and the lattice constant of each monolayer  $a_0 = 3.317 \text{ \AA}$ .

To describe the superconducting state, we construct the unstrained Bogoliubov-de Gennes (BdG) Hamiltonian,

$$\hat{H}_{\text{BdG}} = \begin{pmatrix} \hat{H}_+ & \Delta(\hat{\mathbf{k}}) \\ \Delta^\dagger(\hat{\mathbf{k}}) & -\hat{H}_- \end{pmatrix}, \quad (3)$$

whose eigenstates and eigenvalues are evaluated with keeping only the first-order interlayer coupling to calculate response functions [38]. As for the superconducting order parameter, we consider both the chiral and nematic states as the promising candidates of superconductivity in tWSe<sub>2</sub> [4, 5], which are given by  $\Delta(\mathbf{k}) = \Delta(T)(k_x^2 - k_y^2 + 2ik_x k_y)/k^2$  and  $\Delta(T)(k_x^2 - k_y^2)/k^2$ , respectively, with  $k = |\mathbf{k}|$ . The gap amplitude is assumed to have a phenomenological temperature dependence  $\Delta(T) = \Delta_0 \tanh \left[ 1.74 \sqrt{\frac{T_c}{T}} - 1 \right]$  with  $\Delta_0 = 1.76 k_B T_c$ , where  $T_c = 0.426 \text{ K}$  is the critical temperature for the twist angle  $5.0^\circ$  [3].

*SAWs and pseudo-gauge fields.*— To discuss superconducting SAWs responses, we consider SAWs propagating along the surface of the tWSe<sub>2</sub> [see Fig. 1], introducing a spatio-temporally periodic strain in the crystal lattice. In particular, we focus on the Rayleigh-type SAWs, which can be easily excited under traction-free boundary conditions on piezoelectric substrates [39]. The Rayleigh-type SAWs propagating on the surface of a piezoelectric substrates in the  $xy$  plane are described by the displacement field  $\mathbf{u}(\mathbf{r}, t) = \text{Re} \left[ (u_L \hat{Q} + iu_z \hat{z}) e^{i(\mathbf{Q} \cdot \mathbf{r} - \Omega t)} \right]$ . Here,  $u_L$  and  $u_z$  are the longitudinal and the out-of-plane components,  $\mathbf{Q} = Q\hat{Q} = Q(-\sin\varphi, \cos\varphi)$  is the in-plane propagating wave vector with  $\varphi$  being an azimuthal angle, and  $\Omega$  is the frequency of SAWs applied to tWSe<sub>2</sub>.

When an inhomogeneous strain is applied to honeycomb lattices, a spatial modulation of the lattice is incorporated into the Hamiltonian as the pseudo-gauge fields [21–34, 40]. Assuming that the tWSe<sub>2</sub> on a piezoelectric substrate completely follows the displacement of the substrate, the Rayleigh-type SAWs-induced pseudo-gauge field reads

$$\mathbf{A}_s(\mathbf{r}, t) = \frac{\hbar}{e} \frac{\beta}{2a_0} u_L Q \begin{pmatrix} \sin 2\varphi \\ \cos 2\varphi \end{pmatrix} \text{Im} \left[ e^{i(\mathbf{Q} \cdot \mathbf{r} - \Omega t)} \right], \quad (4)$$

where  $\xi$  is a constant characterizing the SAWs dispersion as  $\Omega = c_t \xi Q$  [41]. This gives rise to the pseudo-electric field  $\mathbf{E}_s(\mathbf{r}, t) = -\partial_t \mathbf{A}_s(\mathbf{r}, t)$ , which oscillates along a certain direction similarly to linearly-polarized light. Note that the pseudo-electric fields stemming from the out-of-plane displacement are proportional to  $u_z^2$ , which are

less relevant under weak strain, and hence neglected in the following analysis.

The strain-induced pseudo-gauge field  $\mathbf{A}_s$  is coupled to the valley DOF rather than charge DOF, working at the two valley points in the opposite direction:  $H_{\tau,l}(\hat{\mathbf{k}}) \rightarrow H_{\tau,l}(\hat{\mathbf{k}} + \frac{\epsilon}{\hbar} \tau \mathbf{A}_s(\hat{\mathbf{r}}, t))$  in Eq. (1). Its coupling to the BdG Hamiltonian is given by replacing  $\hat{H}_\tau$  in Eq. (3) accordingly. To illustrate this, we consider moiré wave-number representation of  $\hat{H}_{\text{BdG}}$  by assuming a spatially uniform  $\mathbf{A}_s$ , for simplicity:

$$H_{\text{BdG}}(\mathbf{k}) = \begin{pmatrix} H_+(\mathbf{k} + \frac{\epsilon}{\hbar} \mathbf{A}_s) & \Delta(\mathbf{k}) \\ \Delta^\dagger(\mathbf{k}) & -H_-^T(-\mathbf{k} - \frac{\epsilon}{\hbar} \mathbf{A}_s) \end{pmatrix}. \quad (5)$$

This indicates that the pseudo-gauge field couples to BdG Hamiltonian by  $H_{\text{BdG}}(\mathbf{k}) \rightarrow H_{\text{BdG}}(\mathbf{k} + \frac{\epsilon}{\hbar} \mathbf{A}_s)$ , in the same way as the coupling of electromagnetic gauge fields to Bloch electrons, when the  $\mathbf{k}$  dependence of  $\Delta(\mathbf{k})$  is not significant. As a result, the quantum geometry of Bogoliubov quasiparticles is relevant to SAW-induced excitations. This observation stands in sharp contrast to and illustrates the advantage of SAWs over optical responses, where the gauge field couples to  $H_{\text{BdG}}(\mathbf{k})$  with the opposite signs in the electron and hole sectors reflecting their negative and positive charges, and therefore cannot directly capture the quantum geometry of Bogoliubov quasiparticles.

Strictly speaking, the pseudo-gauge field is not the only way strain affects the system, and there exists correction by the strain-induced coordinate transformations [42]. While its spatio-temporal modulation by SAWs may also trigger nontrivial responses, particularly in the presence of heterostrain components in moiré multilayers, we concentrate on the homostrain contributions to the pseudo-gauge field as the primary source and leave the other effects to future issues.

*Superconducting acoustogalvanic effect.*— The pseudo-electric field  $\mathbf{E}_s$  is known to give rise to nonlinear responses in the normal state, referred to as the acoustogalvanic effect (AGE) [25, 29]. In this Letter, we propose its counterpart in the superconducting state, namely the superconducting AGE (SAGE) as a probe of exotic superconductivity in two-dimensional materials. We define the SAGE as the rectification charge current driven by SAWs-induced pseudo-electric fields:

$$\langle \hat{\mathcal{J}}^\alpha \rangle = \sigma_{\mathbf{Q}, -\mathbf{Q}}^{\alpha; \beta\gamma}(0; \Omega, -\Omega) E_s^\beta(\mathbf{Q}, \Omega) E_s^\gamma(-\mathbf{Q}, -\Omega), \quad (6)$$

where  $\langle \hat{\mathcal{J}}^\alpha \rangle$  represents the spatio-temporally uniform charge current and  $\mathbf{E}_s(\mathbf{Q}, \Omega)$  is a Fourier component of the pseudo-electric field. Note that the finite momentum transfer  $\mathbf{Q}$  should be incorporated, since  $Q$  is much larger than that for optical responses due to the difference in speed of sound and light. Note also that only  $(\beta, \gamma)$ -symmetric components contribute among various components of  $\sigma_{\mathbf{Q}, -\mathbf{Q}}^{\alpha; \beta\gamma}$ , since  $\mathbf{E}_s$  is linearly polarized.

Similarly to the nonlinear optical responses [43, 44], the acoustogalvanic conductivity is divided into several contributions with different physical origins. In this Letter, we focus on that corresponds to the injection current, which is expected to be dominant in the clean-limit superconductors and therefore relevant to unconventional superconductivity. By generalizing the derivation of nonlinear optical responses [9], this contribution,  $\sigma_{\text{inj}}^{\alpha; \beta\gamma}$ , is given by

$$\sigma_{\text{inj}}^{\alpha; \beta\gamma} = \frac{-\pi}{2\eta} \int \frac{d^2\mathbf{k}}{(2\pi)^2} \sum_{a,b} (\mathcal{J}_{aa}^\alpha - \mathcal{J}_{bb}^\alpha) G_{ab}^{\beta\gamma} F_{ab}(\Omega). \quad (7)$$

Here, the indices  $a$  and  $b$  specify the eigenstates of  $\hat{H}_{\text{BdG}}$  with the wave numbers  $\mathbf{k} + \mathbf{Q}/2$  and  $\mathbf{k} - \mathbf{Q}/2$ , respectively, while  $E_{ab} = E_a - E_b$ ,  $F_{ab}(\Omega) = [f(E_a) - f(E_b)]\delta(\Omega - E_{ab})$ , and  $G_{ab}^{\beta\gamma} = (V_{ab}^\beta V_{ba}^\gamma + V_{ab}^\gamma V_{ba}^\beta)/2E_{ab}^2$ , with the eigenvalue  $E_a$  and Fermi-Dirac distribution function  $f(E) = (e^{E/k_B T} + 1)^{-1}$ . Throughout, we set  $\hbar = 1$ , and the  $\mathbf{k}$  integral runs over the MBZ. The adiabaticity parameter  $\eta = +0$  will be replaced by the scattering rate  $\Gamma$  for numerical calculations, following the standard procedure for the nonlinear optical responses [9].

The matrix elements such as  $\mathcal{J}_{aa}^\alpha$  and  $V_{ab}^\beta$  represent those for the charge current operator  $\hat{\mathcal{J}}^\alpha$  and its counterpart for the pseudo-gauge field,  $\hat{V}^\beta = \lim_{\mathbf{A}_s \rightarrow 0} (-\partial_{A_s^\beta} \hat{H}_{\text{BdG}})$ . The precise expression of  $V_{ab}^\beta$  with momentum transfer  $\mathbf{Q}$  is available in Supplemental Material. We can replace  $\partial_{A_s^\beta}$  with  $\partial_{k_\beta}$  when  $\partial_{k_\beta} \Delta(\mathbf{k})$  makes negligible contribution to  $G_{ab}^{\beta\gamma}$ , and then  $G_{ab}^{\beta\gamma}$  for  $\mathbf{Q} \rightarrow 0$  coincides with the band-resolved quantum metric of Bogoliubov quasiparticles. This replacement is confirmed to be a good approximation for our model of tWSe<sub>2</sub>, while we use the rigorous expression for numerical calculations. In this way, various quantum-geometric quantities beyond the band-resolved quantum metric are expected to appear in different contributions to acoustogalvanic conductivity, which will be discussed elsewhere.

To understand how  $\sigma_{\text{inj}}^{\alpha; \beta\gamma}$  behaves, we simplify Eq. (7) by keeping single band  $\epsilon_{\mathbf{k}}$  near the Fermi energy and denote the order parameter on it by  $\Delta_{\mathbf{k}}$ . Then, the BdG Hamiltonian Eq. (5) reduces to  $H_{\text{BdG}}(\mathbf{k}) = \epsilon_{\mathbf{k}} \tau_z + \Delta_{\mathbf{k}} \tau_x$  with Pauli matrices  $\tau_z$  and  $\tau_x$ , and  $\sigma_{\text{inj}}^{\alpha; \beta\gamma}$  at  $T = 0$  recasts into

$$\sigma_{\text{inj}}^{\alpha; \beta\gamma} = \frac{\pi Q_{\alpha'}}{2\eta} \int \frac{d^2\mathbf{k}}{(2\pi)^2} \frac{1}{m_{\mathbf{k}}^{\alpha\alpha'}} G^{\beta\gamma}(\mathbf{k}) \delta(\Omega - 2E_{\mathbf{k}}), \quad (8)$$

up to  $O(Q^3)$  terms. Here, we have defined  $G^{\beta\gamma}(\mathbf{k}) = v_{\mathbf{k}}^\beta v_{\mathbf{k}}^\gamma |\Delta_{\mathbf{k}}|^2 / 4E_{\mathbf{k}}^4$ ,  $E_{\mathbf{k}} = \sqrt{\epsilon_{\mathbf{k}}^2 + |\Delta_{\mathbf{k}}|^2}$ ,  $v_{\mathbf{k}}^\beta = \partial_{k_\beta} \epsilon_{\mathbf{k}}$  and  $1/m_{\mathbf{k}}^{\alpha\alpha'} = \partial_{k_\alpha} \partial_{k_{\alpha'}} \epsilon_{\mathbf{k}}$ . When  $\epsilon_{\mathbf{k}}$  is a parabolic band, for example, Eq. (8) is a positive or negative definite tensor depending on the sign of the effective mass. Therefore, a finite SAGE is expected regardless of the pairing symmetry, and serves as a versatile probe of superconducting

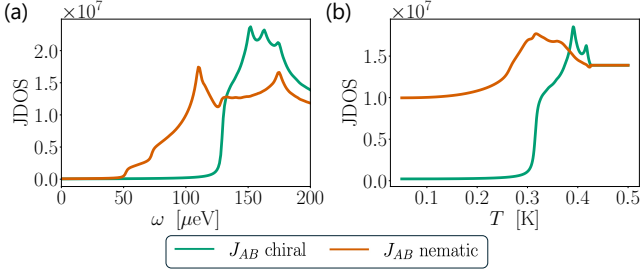


FIG. 3. (a) Frequency and (b) temperature dependencies of JDOS. The green and orange curves correspond to JDOS computed for the chiral and nematic states, respectively.

states in vdW superconductors. In particular, neither inversion nor time-reversal-symmetry breaking is required due to  $\mathbf{Q} \neq 0$ , in contrast to the  $(\beta, \gamma)$ -symmetric optical injection current [9, 43, 44].

*Applications to  $tWSe_2$ .*— We are now ready to investigate the SAGE responses in  $tWSe_2$ . In particular, we discuss the frequency and temperature dependencies of the acoustogalvanic conductivity Eq. (7). Before evaluating these quantities, we analyze the joint density of states (JDOS),

$$J_{ab}(\omega; \mathbf{Q}) = \int \frac{d^2\mathbf{k}}{(2\pi)^2} \delta(E_a - E_b - \omega), \quad (9)$$

which quantifies the number of available resonance transitions at a frequency  $\omega$  between the states  $a$  and  $b$  with the wave numbers  $\mathbf{k} + \mathbf{Q}/2$  and  $\mathbf{k} - \mathbf{Q}/2$ , respectively. JDOS serves as a qualitative guide to the behavior of the response across different frequencies and temperatures.

The numerical results of JDOS are shown in Fig. 3. In our calculation, we label the two bands closest to the Fermi surface as bands A and B. Since we are interested in the superconducting energy scale ranging from MHz to GHz, the dominant contribution is determined by these two bands, namely,  $J_{AB}$ . In the following, we discuss the frequency and temperature dependencies of JDOS for the chiral and nematic states.

We first focus on the frequency dependence of JDOS at a fixed temperature  $T = 50$  mK in Fig. 3(a), which lies well below the critical temperature  $T_c = 0.426$  K and thus  $\Delta(T) \simeq \Delta_0$ . Here and hereafter, we adopt  $2\pi/Q = \lambda_{SAW} = 0.4 \mu\text{m}$ , which corresponds to SAWs with frequency  $\Omega = 10$  GHz. Since the superconducting gap is estimated to be  $\Delta_0 \simeq 64 \mu\text{eV}$  in  $tWSe_2$ , the resonance at  $\omega = 2\Delta_0$  is manifested as the typical frequency where JDOS begins to have sizable values. In the chiral state, where a fully-gapped state is realized, JDOS exhibits a vanishing response below the resonance and a sharp peak at  $\omega = 2\Delta_0$ . On the other hand, in the nematic state, a finite JDOS persists even below the resonance frequency due to its nodal gap structure.

The temperature dependence of JDOS with a fixed frequency  $\Omega = 100 \mu\text{eV}$  is shown in Fig. 3(b). The JDOS

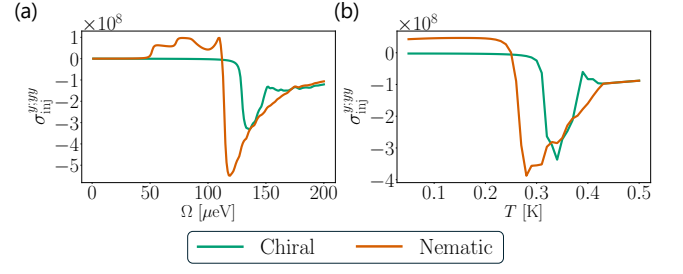


FIG. 4. Frequency (a) and temperature (b) dependencies of the superconducting acoustogalvanic response  $\sigma_{\text{inj}}^{y:yy}$  for chiral and nematic superconducting states. In the chiral state (green line), a strong peak appears when the resonance condition  $\Omega \approx 2\Delta(T)$ , is met. In contrast, the nematic state (orange line) exhibits finite responses even when  $\Omega < 2\Delta(T)$  due to its low-energy quasiparticles. We adopt  $T = 50$  mK for panel (a).

increases toward the resonance near  $\Omega = 2\Delta(T)$  in both the chiral and nematic states by decreasing the temperature. Beyond the resonance, their behaviors diverge significantly. In the chiral state, the JDOS rapidly diminishes due to its fully-gapped structure. On the other hand, in the nematic state, its nodal structure retains a finite JDOS even beyond the resonance, as quasiparticles can still resonate near the nodes.

Based on the insight of JDOS, we discuss the SAGE in  $tWSe_2$ . By assuming SAWs directed along  $\varphi = 0$ , both  $\mathbf{Q}$  and  $\mathbf{E}_s$  are parallel to the  $y$  axis, and then we focus on  $\sigma_{\text{inj}}^{y:yy}$  for the chiral and nematic states. Fig. 4 shows the frequency and temperature dependencies of the acoustogalvanic conductivity  $\sigma_{\text{inj}}^{y:yy}$  for the chiral and nematic states at the same fixed parameters with Fig. 3. We should note that  $Q$  is fixed for any frequency  $\Omega$  of SAWs in Fig. 4(a), to make it easier to compare the results with JDOS in Fig. 3(a). In reality, a slight suppression is expected in the low frequency range since  $Q$  scales with  $\Omega$ .

According to Fig. 4(a), the response of the chiral state is suppressed in the low-frequency regime due to the full-gap structure. As the frequency approaches the resonance frequency  $\Omega = 2\Delta_0$ ,  $\sigma_{\text{inj}}^{y:yy}$  first shows a resonant peak as in JDOS. The nematic state also follows JDOS, and has finite responses even at frequency smaller than  $2\Delta_0$  owing to the presence of low-energy quasiparticles. The sign reversal of SAGE at  $\Omega \sim 110 \mu\text{eV}$  can be understood based on Eq. (8): As detailed in Supplemental Material, the system has two Fermi surfaces which have effective masses  $m_{yy}(\mathbf{k})$  of different signs. The Fermi surface governing  $\sigma_{\text{inj}}^{y:yy}$  switches at  $\Omega \sim 110 \mu\text{eV}$ , leading to the sign reversal in the nematic state.

The temperature dependence of the acoustogalvanic conductivity can be understood in a similar manner. In the chiral state, a finite response emerges only at temperatures where the resonance condition is satisfied, i.e.,

when the JDOS becomes non-zero. The response vanishes after  $2\Delta(T)$  grows and exceeds  $\Omega$ . On the other hand, a finite response is always observed below the critical temperature in the nematic state, with a sign reversal for the same reason as that of Fig. 4(a). The different temperature dependence of SAGE will serve as a strong probe of the low-energy excitations, and therefore has the potential to experimentally distinguish the nematic and chiral states. Thus, our SAGE opens a new avenue for identifying unconventional superconducting states in moiré materials and beyond.

*Discussion.*— Finally, we discuss the experimental feasibility of the SAGE. In a realistic experimental condition, the amplitude of charge current is estimated to be of the order of  $100 \text{ nA/nm}^2$  with the pseudo-electric field  $|\mathbf{E}_s| \simeq 1.5 \times 10^3 \text{ V/m}$  induced by the Rayleigh-type SAWs, as well as a phenomenological scattering rate  $\Gamma = 2\Delta_0/100$  (See Supplemental Materials). Here, we have used the parameters [42, 45, 46]:  $u_L \simeq 100 \text{ pm}$ ,  $c_t \simeq 4000 \text{ m/s}$ ,  $\xi \simeq 0.95$ ,  $\beta \sim 2.3$ , and  $\hbar\Omega = 100 \mu\text{eV}$ , which coincides with  $\Omega/2\pi \sim 25 \text{ GHz}$ . The corresponding wave length  $\lambda_{\text{SAW}} \simeq 160 \text{ nm}$  is comparable to the coherence length of tWSe<sub>2</sub> ( $\sim 57 \text{ nm}$  [3]), highlighting the significance of the momentum transfer  $Q$  in SAGE. Generally speaking, elastic substrates such as LiNbO<sub>3</sub> also generate a piezoelectric field, inducing the acoustoelectric effect [16–18]. In practice, however, this effect can be suppressed by inserting a dielectric sheet such as hBN between the piezoelectric substrate and the moiré superconductor, which is particularly suitable for vdW materials. Therefore, we can only investigate the SAGE and ignore other contributions.

Most candidates of exotic superconductors exhibit extremely low critical temperatures, typically ranging from 0.1 to 1 K, with superconducting gaps estimated to be on the order of  $10^{1-2} \mu\text{eV}$ . This energy scale lies outside the accessible range of the conventional optical spectroscopy. In contrast, SAWs operate in the MHz to GHz range, serving our SAGE as a powerful and suitable tool for probing such low-energy excitations and gap structures.

We discuss future perspectives of SAGE. We first point out that SAGE may distinguish the inter- and intra-valley pairings. While we have studied the inter-valley pairing, the pseudo-gauge field  $\mathbf{A}_s$  couples in the same way as the electromagnetic gauge field for the case of intra-valley pairing, and thus completely different responses are expected. Second, we can probe the spontaneous rotational symmetry breaking of the nematic state by comparing the longitudinal responses along the  $\hat{y}$  direction and that in the  $C_3\hat{y}$  direction. Third, while we have concentrated on the SAGE conductivity corresponding to the injection current, there are other contributions subleading in terms of the scattering rate. They would be certainly related to the quantum geometry of Bogoliubov quasiparticles beyond the band-resolved quantum metric. We leave these as interesting future issues.

In summary, we have developed a fundamental framework for nonlinear responses in atomically thin superconductors driven by SAWs dubbed the superconducting acoustogalvanic effect (SAGE). We have further proposed this SAGE as a novel probe for the gap structure and the quantum geometry of exotic superconductors, such as MATBG and tWSe<sub>2</sub>. In stark contrast to optical responses, our SAGE permits direct access to the quantum geometry of Bogoliubov quasiparticles, and thus will pave the way toward the experimental identification of exotic superconducting states in vdW materials.

The authors are grateful to K. Shinada, H. Tanaka, S. Asano, and Y. Hirobe for fruitful discussions. R.S. thanks Y. Ominato and M. Matsuo for their introduction to the strain gauge fields and SAWs. This work was supported by JST SPRING (Grant Number JPMJSP2110) and JSPS KAKENHI (Grants No.JP22KJ1937, No.JP22H01181, No.JP22H04933, No.JP23K17353, No.JP23K22452, No.JP23KK0248, No.JP24H00007, No.JP24H01662, No.JP24K21530, and No.JP25H01249).

---

\* [matsumoto.tsugumi.78w@st.kyoto-u.ac.jp](mailto:matsumoto.tsugumi.78w@st.kyoto-u.ac.jp)

- [1] Y. Cao, V. Fatemi, S. Fang, K. Watanabe, T. Taniguchi, E. Kaxiras, and P. Jarillo-Herrero, Unconventional superconductivity in magic-angle graphene superlattices, *Nature* **556**, 43 (2018).
- [2] Y. Xia, Z. Han, K. Watanabe, T. Taniguchi, J. Shan, and K. F. Mak, Superconductivity in twisted bilayer WSe<sub>2</sub>, *Nature* **637**, 833 (2025).
- [3] Y. Guo, J. Pack, J. Swann, L. Holtzman, M. Cothrine, K. Watanabe, T. Taniguchi, D. G. Mandrus, K. Barmak, J. Hone, A. J. Millis, A. Pasupathy, and C. R. Dean, Superconductivity in 5.0° twisted bilayer WSe<sub>2</sub>, *Nature* **637**, 839 (2025).
- [4] C. Schrade and L. Fu, Nematic, chiral, and topological superconductivity in twisted transition metal dichalcogenides, *Phys. Rev. B* **110**, 035143 (2024).
- [5] D. Guerzi, D. Kaplan, J. Ingham, J. H. Pixley, and A. J. Millis, Topological superconductivity from repulsive interactions in twisted WSe<sub>2</sub>, arXiv [cond-mat.supr-con] (2024), [arXiv:2408.16075 \[cond-mat.supr-con\]](https://arxiv.org/abs/2408.16075).
- [6] Y. Tokura and N. Nagaosa, Nonreciprocal responses from non-centrosymmetric quantum materials, *Nat. Commun.* **9**, 3740 (2018).
- [7] N. Nagaosa and Y. Yanase, Nonreciprocal transport and optical phenomena in quantum materials, *Annu. Rev. Condens. Matter Phys.* **15**, 63 (2024).
- [8] Z. Wang, L. Dong, C. Xiao, and Q. Niu, Berry curvature effects on quasiparticle dynamics in superconductors, *Phys. Rev. Lett.* **126**, 187001 (2021).
- [9] H. Watanabe, A. Daido, and Y. Yanase, Nonreciprocal optical response in parity-breaking superconductors, *Phys. Rev. B* **105**, 024308 (2022).
- [10] H. Watanabe, A. Daido, and Y. Yanase, Nonreciprocal meissner response in parity-mixed superconductors, *Phys. Rev. B* **105**, L100504 (2022).

- [11] H. Tanaka, H. Watanabe, and Y. Yanase, Nonlinear optical responses in noncentrosymmetric superconductors, *Phys. Rev. B Condens. Matter* **107**, 024513 (2023).
- [12] H. Tanaka, H. Watanabe, and Y. Yanase, Nonlinear optical response in superconductors in magnetic field: Quantum geometry and topological superconductivity, *Phys. Rev. B* **110**, 014520 (2024).
- [13] M. Oles, V. Giovanni, and J. C. W. Song, Superconducting berry curvature dipole, arXiv [cond-mat.supr-con] (2024), arXiv:2410.21363 [cond-mat.supr-con].
- [14] D. Kaplan, K. P. Lucht, P. A. Volkov, and J. H. Pixley, Quantum geometric photocurrents of quasiparticles in superconductors, arXiv [cond-mat.supr-con] (2025), arXiv:2502.12265 [cond-mat.supr-con].
- [15] H. Tanaka and Y. Yanase, Vertex correction for the linear and nonlinear optical responses in superconductors: multiband effect and topological superconductivity, arXiv [cond-mat.supr-con] (2025), arXiv:2502.15373 [cond-mat.supr-con].
- [16] V. I. Fal'ko, V. S. V. Meshkov, and S. V. Iordanskii, Acoustoelectric drag effect in the two-dimensional electron gas at strong magnetic field, *Phys. Rev. B Condens. Matter* **47**, 9910 (1993).
- [17] V. Miseikis, J. E. Cunningham, K. Saeed, R. O'Rorke, and A. G. Davies, Acoustically induced current flow in graphene, *Appl. Phys. Lett.* **100**, 133105 (2012).
- [18] L. Bandhu, L. M. Lawton, and G. R. Nash, Macroscopic acoustoelectric charge transport in graphene, *Appl. Phys. Lett.* **103**, 133101 (2013).
- [19] K. Sonowal, A. V. Kalameitsev, V. M. Kovalev, and I. G. Savenko, Acoustoelectric effect in two-dimensional dirac materials exposed to rayleigh surface acoustic waves, *Phys. Rev. B* **102**, 235405 (2020).
- [20] Y. Mou, J. Wang, H. Chen, Y. Xia, H. Li, Q. Yan, X. Jiang, Y. Wu, W. Shi, H. Jiang, X. C. Xie, and C. Zhang, Coherent detection of the oscillating acoustoelectric effect in graphene, *Phys. Rev. Lett.* **134**, 096301 (2025).
- [21] F. von Oppen, F. Guinea, and E. Mariani, Synthetic electric fields and phonon damping in carbon nanotubes and graphene, *Phys. Rev. B* **80**, 075420 (2009).
- [22] A. Vaezi, N. Abedpour, R. Asgari, A. Cortijo, and M. A. H. Vozmediano, Topological electric current from time-dependent elastic deformations in graphene, *Phys. Rev. B* **88**, 125406 (2013).
- [23] M. A. Cazalilla, H. Ochoa, and F. Guinea, Quantum spin hall effect in two-dimensional crystals of transition-metal dichalcogenides, *Phys. Rev. Lett.* **113**, 077201 (2014).
- [24] A. V. Kalameitsev, V. M. Kovalev, and I. G. Savenko, Valley acoustoelectric effect, *Phys. Rev. Lett.* **122**, 256801 (2019).
- [25] P. O. Sukhachov and H. Rostami, Acoustogalvanic effect in dirac and weyl semimetals, *Phys. Rev. Lett.* **124**, 126602 (2020).
- [26] E. Sela, Y. Bloch, F. von Oppen, and M. B. Shalom, Quantum hall response to time-dependent strain gradients in graphene, *Phys. Rev. Lett.* **124**, 026602 (2020).
- [27] S.-Y. Li, Y. Su, Y.-N. Ren, and L. He, Valley polarization and inversion in strained graphene via pseudo-landau levels, valley splitting of real landau levels, and confined states, *Phys. Rev. Lett.* **124**, 106802 (2020).
- [28] P. Zhao, C. H. Sharma, R. Liang, C. Glasenapp, L. Mouroukh, V. M. Kovalev, P. Huber, M. Prada, L. Tiedemann, and R. H. Blick, Acoustically induced giant synthetic hall voltages in graphene, *Phys. Rev. Lett.* **128**, 256601 (2022).
- [29] P. Bhalla, G. Vignale, and H. Rostami, Pseudogauge field driven acoustoelectric current in two-dimensional hexagonal dirac materials, *Phys. Rev. B* **105**, 125407 (2022).
- [30] B. Uchoa and Y. Barlas, Superconducting states in pseudo-landau-levels of strained graphene, *Phys. Rev. Lett.* **111**, 046604 (2013).
- [31] G. Massarelli, G. Wachtel, J. Y. T. Wei, and A. Paramekanti, Pseudo-landau levels of bogoliubov quasiparticles in strained nodal superconductors, *Phys. Rev. B* **96**, 224516 (2017).
- [32] E. M. Nica and M. Franz, Landau levels from neutral bogoliubov particles in two-dimensional nodal superconductors under strain and doping gradients, *Phys. Rev. B* **97**, 024520 (2018).
- [33] M. M. Nayga, S. Rachel, and M. Vojta, Magnon landau levels and emergent supersymmetry in strained antiferromagnets, *Phys. Rev. Lett.* **123**, 207204 (2019).
- [34] R. Sano, Y. Ominato, and M. Matsuo, Acoustomagnonic spin hall effect in honeycomb antiferromagnets, *Phys. Rev. Lett.* **132**, 236302 (2024).
- [35] F. Wu, T. Lovorn, E. Tutuc, I. Martin, and A. H. MacDonald, Topological insulators in twisted transition metal dichalcogenide homobilayers, *Phys. Rev. Lett.* **122**, 086402 (2019).
- [36] T. Devakul, V. Crépel, Y. Zhang, and L. Fu, Magic in twisted transition metal dichalcogenide bilayers, *Nat. Commun.* **12**, 6730 (2021).
- [37] J. Zhu, Y.-Z. Chou, M. Xie, and S. Das Sarma, Superconductivity in twisted transition metal dichalcogenide homobilayers, *Phys. Rev. B* **111**, L060501 (2025).
- [38] See the Supplemental Material.
- [39] X. Nie, X. Wu, Y. Wang, S. Ban, Z. Lei, J. Yi, Y. Liu, and Y. Liu, Surface acoustic wave induced phenomena in two-dimensional materials, *Nanoscale Horiz* **8**, 158 (2023).
- [40] J.-X. Hu, C.-P. Zhang, Y.-M. Xie, and K. T. Law, Nonlinear hall effects in strained twisted bilayer WSe<sub>2</sub>, *Commun. Phys.* **5**, 1 (2022).
- [41] L. D. Landau, E. M. Lifshitz, A. M. Kosevich, and L. P. Pitaevskii, *Theory of elasticity: volume 7, Course of theoretical physics* (Elsevier Science, Kidlington, England, 1986).
- [42] Z. Bi, N. F. Q. Yuan, and L. Fu, Designing flat bands by strain, *Phys. Rev. B* **100**, 035448 (2019).
- [43] J. Ahn, G.-Y. Guo, and N. Nagaosa, Low-frequency divergence and quantum geometry of the bulk photovoltaic effect in topological semimetals, *Phys. Rev. X* **10**, 041041 (2020).
- [44] H. Watanabe and Y. Yanase, Chiral photocurrent in parity-violating magnet and enhanced response in topological antiferromagnet, *Phys. Rev. X* **11**, 011001 (2021).
- [45] S. Fang, S. Carr, M. A. Cazalilla, and E. Kaxiras, Electronic structure theory of strained two-dimensional materials with hexagonal symmetry, *Phys. Rev. B* **98**, 075106 (2018).
- [46] A. A. Maznev, R. Mincigrucci, F. Bencivenga, V. Unikan-danunni, F. Capotondi, G. Chen, Z. Ding, R. A. Duncan, L. Foglia, M. G. Izzo, C. Masciovecchio, A. Martinelli, G. Monaco, E. Pedersoli, S. Bonetti, and K. A. Nelson, Generation and detection of 50 GHz surface acoustic waves by extreme ultraviolet pulses, *Appl. Phys. Lett.* **119**, 044102 (2021).

## Supplemental Material

### Moiré wave-number representation of the continuum model

In this section, we introduce the moiré wave-number representation of the continuum model. The original continuum model is given by

$$H_\tau = \int d\mathbf{r} \Psi_\tau^\dagger(\mathbf{r}) \begin{pmatrix} \hat{H}_{\tau,b}(\hat{\mathbf{k}}) + \Delta_b(\mathbf{r}) & T_\tau(\mathbf{r}) \\ T_\tau^\dagger(\mathbf{r}) & \hat{H}_{\tau,t}(\hat{\mathbf{k}}) + \Delta_t(\mathbf{r}) \end{pmatrix} \Psi_\tau(\mathbf{r}), \quad (10)$$

where the components are given by

$$\hat{H}_{\tau,l}(\hat{\mathbf{k}}) = -\frac{\hbar^2}{2m^*} (\hat{\mathbf{k}} - \boldsymbol{\kappa}_{\tau,l})^2 - l \frac{V_z}{2}, \quad (11)$$

$$\Delta_l(\mathbf{r}) = V \sum_{j=1,2,3} e^{i(\mathbf{g}_j \cdot \mathbf{r} + l\psi)} + \text{h.c.}, \quad (12)$$

$$T_\tau(\mathbf{r}) = w(1 + e^{+i\tau\mathbf{g}_2 \cdot \mathbf{r}} + e^{-i\tau\mathbf{g}_3 \cdot \mathbf{r}}). \quad (13)$$

We define the Fourier transformation of the field operator by

$$\psi_l^\dagger(\mathbf{r}) = \int_{-\infty}^{\infty} \frac{d\mathbf{k}}{\sqrt{(2\pi)^2}} e^{-i\mathbf{k} \cdot \mathbf{r}} c_l^\dagger(\mathbf{k}), \quad (14)$$

and obtain

$$\begin{aligned} H_m^\tau &= \int d\mathbf{r} \psi_l^\dagger(\mathbf{r}) \hat{H}_{\tau,l}(-i\nabla) \psi_l(\mathbf{r}) \\ &= \int_{-\infty}^{\infty} \frac{d\mathbf{k}}{(2\pi)^2} c_l^\dagger(\mathbf{k}) H_{\tau,l}(\mathbf{k}) c_l(\mathbf{k}), \end{aligned} \quad (15)$$

$$\begin{aligned} H_\Delta^\tau &= \int d\mathbf{r} \psi_l^\dagger(\mathbf{r}) \Delta_l(\mathbf{r}) \psi_l(\mathbf{r}) \\ &= V e^{il\psi} \sum_{j=1,2,3} \int d\mathbf{r} \psi_l^\dagger(\mathbf{r}) e^{i\mathbf{g}_j \cdot \mathbf{r}} \psi_l(\mathbf{r}) + \text{h.c.} \\ &= \int_{-\infty}^{\infty} \frac{d\mathbf{k}}{(2\pi)^2} V \sum_j \left[ e^{+il\psi} c_l^\dagger(\mathbf{k} + \mathbf{g}_j) c_l(\mathbf{k}) + e^{-il\psi} c_l^\dagger(\mathbf{k}) c_l(\mathbf{k} + \mathbf{g}_j) \right], \end{aligned} \quad (16)$$

$$\begin{aligned} H_T^\tau &= \int d\mathbf{r} \psi_b^\dagger(\mathbf{r}) T_\tau(\mathbf{r}) \psi_t(\mathbf{r}) + \text{h.c.} \\ &= \int d\mathbf{r} \psi_b^\dagger(\mathbf{r}) w(1 + e^{-i\tau\mathbf{g}_2 \cdot \mathbf{r}} + e^{+i\tau\mathbf{g}_3 \cdot \mathbf{r}}) \psi_t(\mathbf{r}) + \text{h.c.} \\ &= w \int_{-\infty}^{\infty} \frac{d\mathbf{k}}{(2\pi)^2} \left[ c_b^\dagger(\mathbf{k}) c_t(\mathbf{k}) + c_b^\dagger(\mathbf{k}) c_t(\mathbf{k} - \tau\mathbf{g}_2) + c_b^\dagger(\mathbf{k} - \tau\mathbf{g}_3) c_t(\mathbf{k}) \right] + \text{h.c.}, \end{aligned} \quad (17)$$

where  $\mathbf{g}_j = \frac{4\pi}{\sqrt{3}L_M} \left( \cos \frac{2(j-1)\pi}{3}, \sin \frac{2(j-1)\pi}{3} \right)$  represents moiré reciprocal lattice vectors. In this work, we only consider the first-order interlayer coupling, then, we choose the basis as

$$\Psi_b(\mathbf{k}) = (c_b(\mathbf{k}), c_b(\mathbf{k} + \mathbf{g}_1), c_b(\mathbf{k} - \mathbf{g}_3)), \quad (18)$$

$$\Psi_t(\mathbf{k}) = (c_t(\mathbf{k}), c_t(\mathbf{k} + \mathbf{g}_1), c_t(\mathbf{k} - \mathbf{g}_2)), \quad (19)$$

by keeping the states near the original massive Dirac cones of the bottom and top layers, respectively. Here,  $\mathbf{k}$  represents the wave number in the moiré Brillouin zone (MBZ). In the following discussion, we focus on the valley  $\tau = +$ . By rewriting  $H_m$  as

$$H_m^+ = \int_{-\infty}^{\infty} \frac{d\mathbf{k}}{(2\pi)^2} c_l^\dagger(\mathbf{k}) H_l(\mathbf{k}) c_l(\mathbf{k}) \quad (20)$$

$$= \sum_{n,m \in \mathbb{Z}} \int_{\text{MBZ}} \frac{d\mathbf{k}}{(2\pi)^2} c_l^\dagger(\mathbf{k} + n\mathbf{g}_1 + m\mathbf{g}_2) H_l(\mathbf{k} + n\mathbf{g}_1 + m\mathbf{g}_2) c_l(\mathbf{k} + n\mathbf{g}_1 + m\mathbf{g}_2), \quad (21)$$

and keeping the states specified by  $\Psi_b(\mathbf{k})$  and  $\Psi_t(\mathbf{k})$ , we obtain  $H_m^+ = H_m^b + H_m^t$  with

$$H_m^b = \int_{\text{MBZ}} \frac{d\mathbf{k}}{(2\pi)^2} \Psi_b^\dagger(\mathbf{k}) \begin{pmatrix} H_b(\mathbf{k}) & 0 & 0 \\ 0 & H_b(\mathbf{k} + \mathbf{g}_1) & 0 \\ 0 & 0 & H_b(\mathbf{k} - \mathbf{g}_3) \end{pmatrix} \Psi_b(\mathbf{k}) \equiv \int_{\text{MBZ}} \frac{d\mathbf{k}}{(2\pi)^2} \Psi_b^\dagger(\mathbf{k}) h_m^b(\mathbf{k}) \Psi_b(\mathbf{k}), \quad (22)$$

$$H_m^t = \int_{\text{MBZ}} \frac{d\mathbf{k}}{(2\pi)^2} \Psi_t^\dagger(\mathbf{k}) \begin{pmatrix} H_t(\mathbf{k}) & 0 & 0 \\ 0 & H_t(\mathbf{k} + \mathbf{g}_1) & 0 \\ 0 & 0 & H_t(\mathbf{k} - \mathbf{g}_2) \end{pmatrix} \Psi_t(\mathbf{k}) \equiv \int_{\text{MBZ}} \frac{d\mathbf{k}}{(2\pi)^2} \Psi_t^\dagger(\mathbf{k}) h_m^t(\mathbf{k}) \Psi_t(\mathbf{k}). \quad (23)$$

Here and hereafter in this Supplemental Material, we represent the integral over the MBZ by  $\int_{\text{MBZ}} \frac{d\mathbf{k}}{(2\pi)^2}$  to emphasize the difference from  $\int_{-\infty}^{\infty} \frac{d\mathbf{k}}{(2\pi)^2}$ , instead of  $\int \frac{d\mathbf{k}}{(2\pi)^2}$  adopted in the main text. To rewrite  $H_\Delta(j)$  and  $H_T(j)$ , we introduce the decomposition

$$H_\Delta = \sum_j H_\Delta(j), \quad (24)$$

$$H_T = \sum_j H_T(j), \quad (25)$$

and then, each components are give by

$$\begin{aligned} H_\Delta(1) &= \int_{-\infty}^{\infty} \frac{d\mathbf{k}}{(2\pi)^2} V e^{+i\psi} c_l^\dagger(\mathbf{k} + \mathbf{g}_1) c_l(\mathbf{k}) + \text{h.c.} \\ &= \int_{\text{MBZ}} \frac{d\mathbf{k}}{(2\pi)^2} V e^{+i\psi} c_l^\dagger(\mathbf{k} + \mathbf{g}_1) c_l(\mathbf{k}) + \text{h.c.} + (\text{other } \mathbf{k}), \end{aligned} \quad (26)$$

$$\begin{aligned} H_\Delta(2) &= \int_{-\infty}^{\infty} \frac{d\mathbf{k}}{(2\pi)^2} V e^{+i\psi} c_l^\dagger(\mathbf{k} + \mathbf{g}_2) c_l(\mathbf{k}) + \text{h.c.} \\ &= \int_{-\infty}^{\infty} \frac{d\mathbf{k}}{(2\pi)^2} V e^{+i\psi} c_l^\dagger(\mathbf{k}) c_l(\mathbf{k} - \mathbf{g}_2) + \text{h.c.} \\ &= \int_{\text{MBZ}} \frac{d\mathbf{k}}{(2\pi)^2} V e^{+i\psi} \left[ c_l^\dagger(\mathbf{k}) c_l(\mathbf{k} - \mathbf{g}_2) + c_l^\dagger(\mathbf{k} - \mathbf{g}_3) c_l(\mathbf{k} + \mathbf{g}_1) \right] + \text{h.c.} + (\text{other } \mathbf{k}), \end{aligned} \quad (27)$$

$$\begin{aligned} H_\Delta(3) &= \int_{-\infty}^{\infty} \frac{d\mathbf{k}}{(2\pi)^2} V e^{+i\psi} c_l^\dagger(\mathbf{k} + \mathbf{g}_3) c_l(\mathbf{k}) + \text{h.c.} \\ &= \int_{-\infty}^{\infty} \frac{d\mathbf{k}}{(2\pi)^2} V e^{+i\psi} c_l^\dagger(\mathbf{k}) c_l(\mathbf{k} - \mathbf{g}_3) + \text{h.c.} \\ &= \int_{\text{MBZ}} \frac{d\mathbf{k}}{(2\pi)^2} V e^{+i\psi} \left[ c_l^\dagger(\mathbf{k}) c_l(\mathbf{k} - \mathbf{g}_3) + c_l^\dagger(\mathbf{k} - \mathbf{g}_2) c_l(\mathbf{k} + \mathbf{g}_1) \right] + \text{h.c.} + (\text{other } \mathbf{k}), \end{aligned} \quad (28)$$

and

$$\begin{aligned} H_T(1) &= \int_{-\infty}^{\infty} \frac{d\mathbf{k}}{(2\pi)^2} w c_b^\dagger(\mathbf{k}) c_t(\mathbf{k}) + \text{h.c.} \\ &= \int_{\text{MBZ}} \frac{d\mathbf{k}}{(2\pi)^2} w \left[ c_b^\dagger(\mathbf{k}) c_t(\mathbf{k}) + c_b^\dagger(\mathbf{k} + \mathbf{g}_1) c_t(\mathbf{k} + \mathbf{g}_1) \right. \\ &\quad \left. + c_b^\dagger(\mathbf{k} - \mathbf{g}_3) c_t(\mathbf{k} - \mathbf{g}_3) + c_b^\dagger(\mathbf{k} - \mathbf{g}_2) c_t(\mathbf{k} - \mathbf{g}_2) \right] + \text{h.c.} + (\text{other } \mathbf{k}), \end{aligned} \quad (29)$$

$$\begin{aligned} H_T(2) &= \int_{-\infty}^{\infty} \frac{d\mathbf{k}}{(2\pi)^2} w c_b^\dagger(\mathbf{k} + \mathbf{g}_2) c_t(\mathbf{k}) + \text{h.c.} \\ &= \int_{\text{MBZ}} \frac{d\mathbf{k}}{(2\pi)^2} w \left[ c_b^\dagger(\mathbf{k}) c_t(\mathbf{k} - \mathbf{g}_2) + c_b^\dagger(\mathbf{k} - \mathbf{g}_3) c_t(\mathbf{k} + \mathbf{g}_1) \right] + \text{h.c.} + (\text{other } \mathbf{k}), \end{aligned} \quad (30)$$

$$\begin{aligned} H_T(3) &= \int_{-\infty}^{\infty} \frac{d\mathbf{k}}{(2\pi)^2} w c_b^\dagger(\mathbf{k} - \mathbf{g}_3) c_t(\mathbf{k}) + \text{h.c.} \\ &= \int_{\text{MBZ}} \frac{d\mathbf{k}}{(2\pi)^2} w \left[ c_b^\dagger(\mathbf{k} - \mathbf{g}_3) c_t(\mathbf{k}) + c_b^\dagger(\mathbf{k} + \mathbf{g}_1) c_t(\mathbf{k} - \mathbf{g}_2) \right] + \text{h.c.} + (\text{other } \mathbf{k}). \end{aligned} \quad (31)$$

Therefore, by keeping the states specified by  $\Psi_b(\mathbf{k})$  and  $\Psi_t(\mathbf{k})$ , we obtain from  $H_m^+$  and  $H_\Delta^+$

$$H_\Delta^b = \int_{\text{MBZ}} \frac{d\mathbf{k}}{(2\pi)^2} \Psi_b^\dagger(\mathbf{k}) \begin{pmatrix} 0 & Ve^{-i\psi} & Ve^{+i\psi} \\ Ve^{+i\psi} & 0 & Ve^{-i\psi} \\ Ve^{-i\psi} & Ve^{+i\psi} & 0 \end{pmatrix} \Psi_b(\mathbf{k}) \equiv \int_{\text{MBZ}} \frac{d\mathbf{k}}{(2\pi)^2} \Psi_b^\dagger(\mathbf{k}) h_\Delta^b(\mathbf{k}) \Psi_b(\mathbf{k}), \quad (32)$$

$$H_\Delta^t = \int_{\text{MBZ}} \frac{d\mathbf{k}}{(2\pi)^2} \Psi_t^\dagger(\mathbf{k}) \begin{pmatrix} 0 & Ve^{+i\psi} & Ve^{-i\psi} \\ Ve^{-i\psi} & 0 & Ve^{+i\psi} \\ Ve^{+i\psi} & Ve^{-i\psi} & 0 \end{pmatrix} \Psi_t(\mathbf{k}) \equiv \int_{\text{MBZ}} \frac{d\mathbf{k}}{(2\pi)^2} \Psi_t^\dagger(\mathbf{k}) h_\Delta^t(\mathbf{k}) \Psi_t(\mathbf{k}), \quad (33)$$

$$H_T = \int_{\text{MBZ}} \frac{d\mathbf{k}}{(2\pi)^2} \Psi_b^\dagger(\mathbf{k}) \begin{pmatrix} w & 0 & w \\ 0 & w & w \\ w & w & 0 \end{pmatrix} \Psi_t(\mathbf{k}) + \text{h.c.} \equiv \int_{\text{MBZ}} \frac{d\mathbf{k}}{(2\pi)^2} \Psi_b^\dagger(\mathbf{k}) h_{bt}(\mathbf{k}) \Psi_t(\mathbf{k}) + \Psi_t^\dagger(\mathbf{k}) h_{tb}(\mathbf{k}) \Psi_b(\mathbf{k}). \quad (34)$$

Thus, we have rewritten Eq. (10) and obtain the moiré wave-number representation

$$H_{\tau=+} = \int_{\text{MBZ}} \frac{d\mathbf{k}}{(2\pi)^2} \left( \Psi_b^\dagger(\mathbf{k}), \Psi_t^\dagger(\mathbf{k}) \right) H_{\tau=+}(\mathbf{k}) \begin{pmatrix} \Psi_b(\mathbf{k}) \\ \Psi_t(\mathbf{k}) \end{pmatrix}, \quad (35)$$

$$H_{\tau=+}(\mathbf{k}) \equiv \begin{pmatrix} h_m^b(\mathbf{k}) + h_\Delta^b(\mathbf{k}) & h_{bt}(\mathbf{k}) \\ h_{tb}(\mathbf{k}) & h_m^t(\mathbf{k}) + h_\Delta^t(\mathbf{k}) \end{pmatrix}. \quad (36)$$

We can also obtain that for  $\tau = -$  and the BdG Hamiltonian in the same way.

#### Details of the numerical calculations and the sign reversal of $\sigma_{\text{inj}}^{y:yy}$

Here, we discuss the details of the numerical calculations. In particular, we explain how the sign reversal of  $\sigma_{\text{inj}}^{y:yy}$  in Fig. 4(a) occurs in the nematic state.

For numerical calculations, delta functions in JDOS and  $\sigma_{\text{inj}}^{y:yy}$  are approximated by the Lorentzian  $\mathcal{L}(x) = \frac{1}{\pi} \frac{\Gamma}{x^2 + \Gamma^2}$ . Here, following Ref. [9], we adapted the same value of  $\Gamma$  as the scattering rate, which is introduced by replacing the adiabaticity parameter  $\eta$  of  $\sigma_{\text{inj}}^{y:yy}$  as discussed in the main text. We determined the value of the scattering rate  $\Gamma$  in the following way. According to Ref. [3], the mean-free path and coherence length are  $l = 229\text{nm}$  and  $\xi_0 = 57\text{nm}$ , where  $l \gg \xi_0$  indicates that the system is in the clean limit. By assuming the relations  $\xi_0 = \hbar v_F / \pi \Delta_0$ ,  $l = v_F / \Gamma_N$ , and with a typical value of the Fermi velocity  $v_F$ , we obtain the normal-state scattering rate  $\Gamma_N \sim 50.5\mu\text{eV}$ , which amounts to  $\sim \Delta_0/2$ . The scattering rate in the superconducting state would be smaller than  $\Gamma_N$  due to the gap opening, and thus we phenomenologically assume a smaller value  $\Gamma = \Delta_0/50 < \Gamma_N$ . We have confirmed that the obtained response is suppressed according to  $\sigma_{\text{inj}}^{y:yy} \sim 1/\Gamma$  by increasing  $\Gamma$  and keep the qualitative temperature dependence intact, as long as  $\Gamma$  is not too large.

As discussed in the main text,  $\sigma_{\text{inj}}^{y:yy}$  of the nematic state shows a sign reversal near  $\Omega \sim 110\mu\text{eV}$ . This behavior can be understood from Eq. (8) and the distributions of the effective mass shown in Fig. 5(b). Figure 5(a) shows the  $\mathbf{k}$  dependence of the excitation energy between the quasiparticle bands  $A, B$ , i.e.,  $E_A(\mathbf{k} + \mathbf{Q}/2) - E_B(\mathbf{k} - \mathbf{Q}/2)$ , in the presence of a finite momentum transfer  $\mathbf{Q}$ . It is evident that the main contributions to the resonance originate from regions near the Fermi surfaces of valley  $+$  in the normal state, which consist of a large open Fermi surface and small Fermi pockets near the moiré K point as indicated by black lines in Fig. 5(b). Note that the acoustogalvanic conductivity  $\sigma_{\text{inj}}^{y:yy}$  can be understood as the summation of the contributions by these large and small Fermi surfaces. According to Eq. (8), the sign of the contribution from each Fermi surface is determined by the effective mass. While the large Fermi surface does not have a definite sign of the effective mass due to the presence of sign reversals, it turns out that the region of  $m^{yy}(\mathbf{k}) < 0$  mainly contributes for the frequency under consideration. Similarly, the small Fermi pockets can be regarded to have positive effective mass. Thus, their contributions to  $\sigma_{\text{inj}}^{y:yy}$  are of different signs. This can be confirmed from Fig. 5(c), where the contributions from large and small Fermi surfaces, indicated by blue and red lines, respectively, have opposite signs. The dominant contribution to the acoustogalvanic conductivity is coming from the small and large Fermi surfaces for small and large frequencies, thereby explaining the sign reversal of  $\sigma_{\text{inj}}^{y:yy}$ .

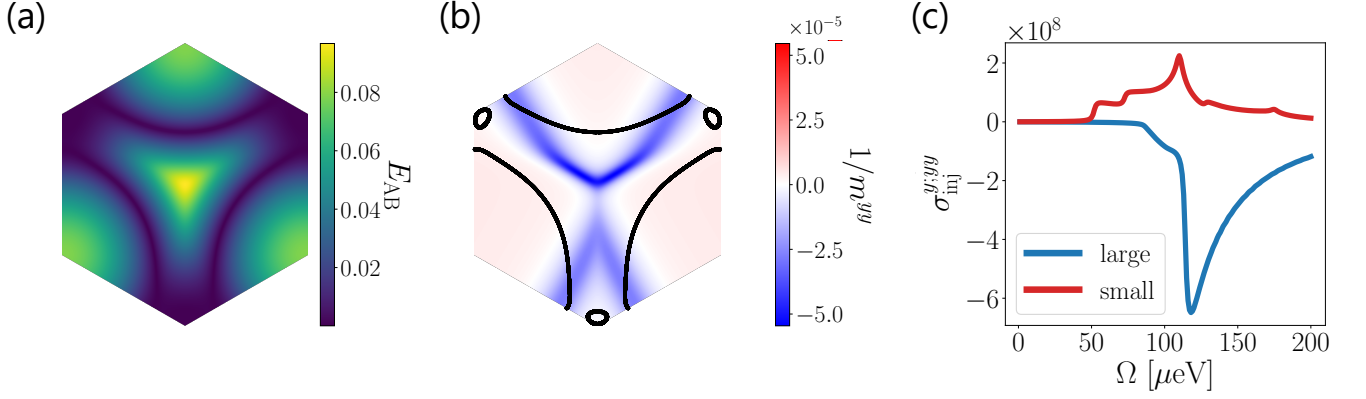


FIG. 5. Color map of (a)  $E_{AB} = E_A(\mathbf{k} + \mathbf{Q}/2) - E_B(\mathbf{k} - \mathbf{Q}/2)$  and (b) the inverse effective mass  $1/m^{yy}(\mathbf{k})$  of the energy band of the + valley near the Fermi energy. In panel (b), the black lines represent the Fermi surfaces of the valley +. (c) Contribution of each Fermi surfaces to  $\sigma_{inj}^{yy}$ . The blue and red lines correspond to large and small Fermi surfaces.

### Formulation of SAGE

Here, we discuss the derivation of the formulas of acoustogalvanic conductivity. In the presence of pseudo-gauge field, the normal-state Hamiltonian of the valley  $\tau$  is written as

$$\hat{H}_\tau[\mathbf{A}_s] = \hat{H}_{\tau,l}[0] - \int \frac{d^2q}{(2\pi)^2} \hat{V}_\tau^{(\beta,\mathbf{q})} A_s^\beta(\mathbf{q}, t) + \frac{1}{2} \int \frac{d^2q}{(2\pi)^2} \int \frac{d^2q'}{(2\pi)^2} \hat{V}_\tau^{(\beta,\mathbf{q})(\gamma,\mathbf{q}')} A_s^\beta(\mathbf{q}, t) A_s^\gamma(\mathbf{q}', t) + O(A_s^3), \quad (37)$$

by using the Fourier coefficients of the pseudo-gauge field,

$$\mathbf{A}_s(\mathbf{r}, t) = \int \frac{d^2q}{(2\pi)^2} e^{i\mathbf{q}\cdot\mathbf{r}} \mathbf{A}_s(\mathbf{q}, t) = \int \frac{d^2q}{(2\pi)^2} \int \frac{d\omega}{2\pi} e^{i\mathbf{q}\cdot\mathbf{r} - i\omega t} \mathbf{A}_s(\mathbf{q}, \omega). \quad (38)$$

Here, the current operators for the pseudo-gauge field is given by  $\hat{V}_\tau^{(\beta,\mathbf{q})} = \text{diag}(\hat{V}_{\tau,b}^{(\beta,\mathbf{q})}, \hat{V}_{\tau,t}^{(\beta,\mathbf{q})})$  and  $\hat{V}_\tau^{(\beta,\mathbf{q})(\gamma,\mathbf{q}')} = \text{diag}(\hat{V}_{\tau,b}^{(\beta,\mathbf{q})(\gamma,\mathbf{q}')}, \hat{V}_{\tau,t}^{(\beta,\mathbf{q})(\gamma,\mathbf{q}')})$ , with

$$\hat{V}_{\tau,l}^{(\beta,\mathbf{q})} = \left\{ -\frac{\tau\hbar^2}{2m^*} (\hat{\mathbf{k}} - \boldsymbol{\kappa}_{\tau,l}), e^{i\mathbf{q}\cdot\hat{\mathbf{r}}} \right\}, \quad \hat{V}_{\tau,l}^{(\beta,\mathbf{q})(\gamma,\mathbf{q}')} = -\frac{\hbar^2\tau^2}{m^*} e^{i(\mathbf{q}+\mathbf{q}')\cdot\hat{\mathbf{r}}} \delta_{\beta\gamma}. \quad (39)$$

Similar expansion is obtained for the BdG Hamiltonian:

$$\hat{H}_{\text{BdG}}[\mathbf{A}_s] = \hat{H}_{\text{BdG}}[0] - \int \frac{d^2q}{(2\pi)^2} \hat{V}^{(\beta,\mathbf{q})} A_s^\beta(\mathbf{q}, t) + \frac{1}{2} \int \frac{d^2q}{(2\pi)^2} \int \frac{d^2q'}{(2\pi)^2} \hat{V}^{(\beta,\mathbf{q})(\gamma,\mathbf{q}')} A_s^\beta(\mathbf{q}, t) A_s^\gamma(\mathbf{q}', t) + O(A_s^3), \quad (40)$$

with  $\hat{V}^{(\beta,\mathbf{q})} = \text{diag}(\hat{V}_+^{(\beta,\mathbf{q})}, -[\hat{V}_-^{(\beta,\mathbf{q})}]^T)$ , and  $\hat{V}^{(\beta,\mathbf{q})(\gamma,\mathbf{q}')} = \text{diag}(\hat{V}_+^{(\beta,\mathbf{q})(\gamma,\mathbf{q}')}, \hat{V}_-^{(\beta,\mathbf{q})(\gamma,\mathbf{q}')})$ . For the latter use, we define

$$\hat{V}^{\bar{\beta}} \equiv \hat{V}^\beta(\mathbf{q} = 0), \quad \hat{V}^{(\beta,\mathbf{q})} = \frac{1}{2} \{ V^\beta, e^{i\mathbf{q}\cdot\hat{\mathbf{r}}} \}. \quad (41)$$

The acoustogalvanic conductivity can be derived by solving the von-Neumann equation for the density matrix with the perturbation  $\mathbf{A}_s(\mathbf{r}, t)$ , in the same way as the nonlinear optical responses. For this purpose, it is convenient to rewrite Eq. (40) in the following form by generalizing the Einstein summation rule:

$$\hat{H}_{\text{BdG}}[\mathbf{A}_s] = \hat{H}_{\text{BdG}} - \hat{V}^{\bar{\beta}} A_s^{\bar{\beta}}(t) + \frac{1}{2} \hat{V}^{\bar{\beta}\bar{\gamma}} A_s^{\bar{\beta}}(t) A_s^{\bar{\gamma}}(t) + O(A_s^3). \quad (42)$$

Here,  $\bar{\beta} = (\beta, \mathbf{q})$  and

$$\hat{V}^{\bar{\beta}} A_s^{\bar{\beta}}(t) \equiv \sum_{\beta} \int \frac{d^2q}{(2\pi)^2} \hat{V}^{(\beta,\mathbf{q})} A_s^\beta(\mathbf{q}, t), \quad (43)$$

for example. By using this notation, we can immediately obtain the acoustogalvanic conductivity based on the results of the optical conductivity [9]. This is achieved by replacing the gauge-field derivative  $\partial_{A^\beta}$  and  $\partial_{A^\gamma}$  with the pseudo-gauge-field derivative  $\partial_{A_s^\beta}$  and  $\partial_{A_s^\gamma}$ . Thus, the acoustogalvanic conductivity corresponding to the injection-current optical response is given by

$$\sigma_{\mathbf{Q}, -\mathbf{Q}}^{\alpha; \beta\gamma}(0; \Omega, -\Omega) = \sigma^{\alpha; \bar{\beta}, \bar{\gamma}}(0; \Omega, -\Omega) = \frac{1}{\Omega^2} \frac{-\pi}{2\eta V} \sum_{ac} \delta \mathcal{J}_{ac}^\alpha V_{ac}^{\bar{\beta}} V_{ca}^{\bar{\gamma}} f_{ac} \delta(\Omega - E_{ac}), \quad \bar{\beta} = (\beta, \mathbf{Q}), \quad \bar{\gamma} = (\gamma, -\mathbf{Q}), \quad (44)$$

with the system area  $V$ . The removal of the overall coefficient  $1/2$  from the expression in Ref. [9] is due to the different conventions of the BdG Hamiltonian: That in Ref. [9] has a twice larger matrix size than that in this paper. In this expression, the indices  $a$  and  $c$  independently run over all the eigenstates of  $\hat{H}_{\text{BdG}}$  including the wave number. The quantities in the summand are defined by  $V_{ac}^{\bar{\beta}} \equiv \langle \psi_a | \hat{V}^{\bar{\beta}} | \psi_c \rangle$  with  $\hat{H}_{\text{BdG}} |\psi_a\rangle = E_a |\psi_a\rangle$ , as well as  $\delta \mathcal{J}_{ac}^\alpha = \mathcal{J}_{aa}^\alpha - \mathcal{J}_{cc}^\alpha$  with  $\mathcal{J}_{aa}^\alpha = \langle \psi_a | \hat{\mathcal{J}}^\alpha | \psi_a \rangle$ . We defined the spatially-uniform charge current operator  $\hat{\mathcal{J}}^\alpha$  by the gauge-field derivative of the BdG Hamiltonian [9]. In particular, we can write  $\hat{\mathcal{J}}^\alpha = \hat{V}^\beta \tau_z$ , with the Pauli matrix  $\tau_z$  in the Nambu space.

Let us redefine  $a$  and  $c$  to represent the band indices of the BdG Hamiltonian, and  $a \rightarrow (\mathbf{k}_a, a)$  and  $c \rightarrow (\mathbf{k}_c, c)$ . Then, the matrix element  $V_{ac}^{\bar{\beta}}$  reduces to

$$V_{ac}^{\bar{\beta}} = \langle \psi_a(\mathbf{k}_a) | \hat{V}^{(\beta, \mathbf{Q})} | \psi_c(\mathbf{k}_c) \rangle = \delta_{\mathbf{k}_a, \mathbf{k}_c + \mathbf{Q}} V_{ac}(\mathbf{k}_a, \mathbf{k}_c), \quad (45)$$

with

$$V_{ac}(\mathbf{k}_a, \mathbf{k}_c) \equiv \left\langle u_a(\mathbf{k}_a) \left| \frac{\hat{V}^\beta(\mathbf{k}_a) + \hat{V}^\beta(\mathbf{k}_c)}{2} \right| u_c(\mathbf{k}_c) \right\rangle. \quad (46)$$

We defined  $\hat{V}^\beta(\mathbf{k}) = e^{-i\mathbf{k} \cdot \hat{\mathbf{r}}} \hat{V}^\beta e^{i\mathbf{k} \cdot \hat{\mathbf{r}}}$  and denoted the Bloch state for the BdG Hamiltonian by  $|\psi_a(\mathbf{k})\rangle = e^{i\mathbf{k} \cdot \hat{\mathbf{r}}} |u_a(\mathbf{k})\rangle$  with its periodic part  $|u_a(\mathbf{k})\rangle$ . By defining

$$\mathcal{J}_{aa}^\alpha(\mathbf{k}_a) \equiv \langle u_a(\mathbf{k}_a) | \hat{\mathcal{J}}^\alpha(\mathbf{k}_a) | u_a(\mathbf{k}_a) \rangle, \quad \hat{\mathcal{J}}^\alpha(\mathbf{k}_a) = e^{-i\mathbf{k}_a \cdot \hat{\mathbf{r}}} \mathcal{J}^\alpha e^{i\mathbf{k}_a \cdot \hat{\mathbf{r}}}, \quad (47)$$

and introducing  $\mathbf{k} = \mathbf{k}_c + \mathbf{Q}/2$ , we obtain

$$\begin{aligned} \sigma_{\text{inj}}^{\alpha; \beta\gamma} &= \frac{\sigma^{\alpha; \bar{\beta}, \bar{\gamma}}(0; \Omega, -\Omega) + (\beta \leftrightarrow \gamma)}{2} \\ &= \frac{1}{2} \frac{-\pi}{2\eta V} \sum_{\mathbf{k}, \mathbf{k}_a, \mathbf{k}_c, a, c} \delta_{\mathbf{k}_a, \mathbf{k} + \frac{\mathbf{Q}}{2}} \delta_{\mathbf{k}_c, \mathbf{k} - \frac{\mathbf{Q}}{2}} (\mathcal{J}_{aa}^\alpha(\mathbf{k}_a) - \mathcal{J}_{cc}^\alpha(\mathbf{k}_c)) \frac{V_{ac}^\beta(\mathbf{k}_a, \mathbf{k}_c) V_{ca}^\gamma(\mathbf{k}_c, \mathbf{k}_a)}{(E_a(\mathbf{k}_a) - E_c(\mathbf{k}_c))^2} \\ &\quad \cdot \left( f(E_a(\mathbf{k}_a)) - f(E_c(\mathbf{k}_c)) \right) \delta(\Omega - E_a(\mathbf{k}_a) + E_c(\mathbf{k}_c)) + (\beta \leftrightarrow \gamma). \end{aligned} \quad (48)$$

By replacing  $(1/V) \sum_{\mathbf{k}}$  with  $\int \frac{d^2 k}{(2\pi)^2}$ , we obtain the formula in the main text.